Main Manuscript for

fMRI-Based CSF Flow Quantification Identifies Cardiac Pulsatility as the Dominant Driver Over Respiratory and Slow Vasomotion Cycles

Pontus Söderström[1], Cecilia Björnfot[2, 3], Britt M. Andersson[1], Jan Malm[4], Anders Eklund[2,3], Anders Wåhlin[1,2,3]

1. Department of Applied Physics and Electronics, Umeå University, S-90187 Umeå, Sweden
2. Department of Diagnostics and Intervention, Biomedical Engineering and Radiation Physics, Umeå University, S-90187 Umeå, Sweden
3. Umeå Center for Functional Brain Imaging (UFBI), Umeå University, S-90187 Umeå, Sweden
4. Department of Clinical Science, Neurosciences, Umeå University, S-90187 Umeå, Sweden

***Corresponding authors:**
Pontus Söderström (pontus.soderstrom@umu.se)
Department of Applied Physics and Electronics, Umeå University, SE 901 87 Umeå, Sweden

Anders Wåhlin (anders.wahlin@umu.se)
Department of Applied Physics and Electronics, Umeå University, SE 901 87 Umeå, Sweden

Keywords: resting-state fMRI, cerebrospinal fluid flow, inflow effect, glymphatic system

This PDF file includes:

Main Text
Figures 1 to 3
Tables 1 to 2

Abstract

Studying cerebrospinal fluid (CSF) flow can reveal physiological and neural drivers of potential importance in brain clearance. CSF flow may be acquired in functional magnetic resonance imaging (fMRI) scans by considering the inflow effect in an edge-slice. Such measurements have large potential considering the broad availability of fMRI, and the already extensive databases focusing on e.g. aging and dementia. However, limiting factors are that the measurements are not quantitative and can rarely separate contributions from different driving mechanisms due to insufficient sampling rate. Here, we present a method that translates fMRI CSF signals into quantitative flow rates associated with cardiac, respiratory and slow-vasomotion cycles, by modeling the spin-history of an oscillating ensemble of molecules. Phantom experiments showed excellent correlations between estimated and true velocities for cardiac- and respiratory-like frequencies, and moderate correlations for a slow vasomotion-like frequency (r = 0.94, 0.97, 0.58 respectively). We also applied the method in a cohort of 48 subjects from the population (68-82 years, 19 women) to characterize CSF flow at the foramen magnum at resting state. These measurements showed a CSF stroke volume of 0.86 [0.61, 1.17] mL for the cardiac, 0.44 [0.25, 0.94] mL for the respiratory, and 0.28 [0.14, 0.45] mL for the slow vasomotion cycle. In conclusion, the method presented here enabled quantitative assessments of CSF flow compatible with typical fMRI acquisitions and showed that the cardiac cycle is a dominant driver of CSF flow.

Main Text

Introduction

Cerebrospinal fluid (CSF) flow oscillations occur in response to cardiac, respiration and low frequency vascular oscillations (1, 2). Measuring this compensatory response can provide important information regarding intracranial compliance (3, 4). Furthermore, CSF pulsation measurements may be informative of the physiological driving forces that can support brain clearance (5). Brain clearance, as currently understood, is performed by the glymphatic system (6, 7) where CSF is suggested to follow perivascular spaces, driven by physiological mechanisms such as cardiac pulsations (8, 9), respiratory-dependent pressure changes (10, 11), as well as slower vascular modulations of neural origin (12, 13). These physiological drivers can be studied in macroscopic CSF regions such as the 4th ventricle and the foramen magnum (14, 15), and while CSF flow in the subarachnoid space is not the same as glymphatic flow, it is still believed to be related (16, 17). In this context, CSF flow at the foramen magnum may be especially informative since it to a greater extent reflects the total volume of CSF displacement that happens in response to cerebrovascular volume changes, as suggested by the Monro-Kellie doctrine (18), compared to the 4th ventricle.

Functional magnetic resonance imaging (fMRI) is a widely used technique to measure neural activity non-invasively, primarily through the detection of blood oxygen level-dependent (BOLD) signals, and large databases from studies focusing on cognition in aging and dementia are already established (19-21). While the main purpose of fMRI is to detect brain activations through local changes in oxygenation concentrations, CSF inflow at edge slices is detectable throughout signal fluctuations. The fMRI signal increases when unsaturated CSF enters the imaging volume, a mechanism called the inflow effect (22). By exploiting the inflow effect, researchers have indirectly measured CSF movement through signal intensity fluctuations (14). These observations have revealed that the change in global BOLD signal is coupled with the CSF flow during sleep, suggesting that CSF dynamics is linked to neural activity while sleeping. Furthermore, a significant coupling between global BOLD and CSF signal changes have also been seen during resting-state fMRI (as typically acquired in the previously mentioned large datasets), where a reduced correlation was associated with neurological disorders such as Alzheimer's (15) and Parkinson's disease (16). These examples, however, have isolated slower frequencies in the CSF flow spectrum, and a quantitative description regarding the importance of slow-waves, respiration and the cardiac-cycle to CSF motion is lacking.

Importantly, the inflow signal is not a direct reflection of instantaneous velocity, but rather the proportion of the fluid that has been replaced since last excitation and the spin-history. The complex dependency on spin-history adds to the challenge of translating the inflow effect to velocity, potentially obscuring true relationships between the physiological cycles and CSF oscillations. This issue becomes of particular significance when the sampling frequency is comparable to, or lower than twice the heart rate. Under such conditions, typical for large-scale fMRI data collections, the inflow signal of cardiac-related flow will be aliased and falsely appear as a low frequency modulation, as the Nyquist criteria is not met (23). Developing a robust method to quantify CSF flow from standard fMRI acquisitions could open new opportunities to investigate the relationship between CSF flow and various cognition- and aging-related metrics that are commonly acquired in ongoing fMRI studies. Such relationships have the potential to provide valuable insights into areas including brain clearance and the progression of neurodegenerative diseases (24).

Here we propose a method that takes spin history into account to quantify CSF flow from the observed inflow effect in fMRI data. The method does not depend on rapid sampling and can be implemented with standard fMRI acquisitions. We validated the method against phantom measurements and applied it to a typical fMRI dataset to quantify the magnitude of cardiac, respiratory and slow vasomotion cycles for CSF flow at the level of foramen magnum, thus

directly addressing the question regarding the importance of different physiological cycles to CSF flow.

Results

CSF flow rates and volumes. The approach to obtain CSF flow quantification in fMRI data was based on simulating the inflow effect by modeling oscillations of an ensemble of molecules and taking their spin-history into account, accounting for excitation-timings of adjacent slices. Oscillations of cardiac, respiratory, and slow vasomotion origin were simultaneously included in the model (through separate cardiac, respiratory and BOLD measurements, respectively) with velocity components that were iteratively updated until the difference between actual and simulated inflow signal was minimized. When applied to a typical whole-brain fMRI data set of N=48 individuals (68-82 years, 19 women), quantitative estimates of the CSF flow at the cranio-cervical junction could be obtained in all subjects. The simulated and measured CSF inflow displayed R^2 values of 0.57 [0.47, 0.67] supporting the appropriateness of the model, see Figure 2A for the distribution of individual R^2 values. Figure 2A also contains the outcome of a negative-control test, where the inflow signal was deliberately matched to cardiac, respiratory and BOLD signals of another subject, illustrating the poor model fit that can be obtained by chance. A typical fit is displayed in Figure 2B (R^2 = 0.64). The estimated velocity amplitudes of the cohort were 12.5 [9.6, 20.0] mm/s for the cardiac component, 1.34 [0.85, 2.35] mm/s for the respiratory component, and 0.19 [0.10, 0.28] mm/s for the slow vasomotion component (Figure 2C). After factoring in the area of the CSF region, the corresponding flow rates and stroke volumes were calculated to be 3.32 [2.77, 5.02] mL/s and 0.86 [0.61, 1.17] mL for the cardiac cycle, 0.34 [0.21, 0.67] mL/s and 0.44 [0.25, 0.94] mL for the respiratory cycle, and 0.052 [0.026, 0.075] mL/s and 0.28 [0.14, 0.45] mL for the slow vasomotion cycle (Figure 2D and 2E).

Model validation. Phantom measurements showed significant correlations between the true and estimated velocities for all three physiological frequencies. We also evaluated the effect of different dispersion rates that was used to mimic a facilitated diffusion phenomena that has been described for CSF (25). The correlation coefficients and linear fits between estimated velocity and the applied pump velocity for all simulations are summarized in Table 2, with all the correlations being statistically significant. The estimated velocities for each of the three frequencies together with the applied pump velocity are displayed in Figure 3A-C for the simulations with a dispersion coefficient of 6.00 cm^2/min.

The estimated mean velocities obtained by fitting a plug flow to the signals of different flow profiles showed strong agreement with the corresponding mean velocities of the underlying flow profiles. The correlation coefficients between the fitted and actual mean velocities were: 0.996 for laminar flow in a cylinder, 0.998 for laminar flow in an annulus. Per design, there was a perfect correlation with plug flow. A summary of these comparisons is presented in Figure 3D.

Discussion

We propose a method to characterize cardiac, respiratory and slow vasomotion velocity components of CSF motion compatible with standard implementations of fMRI acquisitions. Using this method, we could show that CSF flow at the foramen magnum was dominated by cardiac related oscillations, with lower stroke-volumes for the respiratory and slow vasomotion cycles. The method was inspired by recent advancements in utilizing the inflow-related signal enhancements that develop because of CSF oscillations in and out of the imaging volume (e.g. at the fourth ventricle or at the foramen magnum) (14-16). However, the approach presented here provides some major benefits compared to previous studies. Firstly, the method estimated *quantitative* values of CSF velocities, based on a model that does not depend on specific imaging parameters and is verified with phantom experiments. Secondly, using recordings of cardiac and respiration cycles, individual contributions from physiological cycles could be estimated even if sampling frequency did not meet the Nyquist criterion. By this, our approach can easily be integrated to the analysis of existing fMRI datasets.

In the present study we applied the method to analyze CSF flow and stroke volumes at the cranio-cervical junction, where we found median cardiac velocity amplitudes of 12.5 mm/s and respiratory velocity amplitudes of 1.34 mm/s. Previous literature has reported CSF velocities and stroke volumes in this region using PC-MRI; with cardiac velocities by Yildiz et al. 2017 and 2022 to be 9.7 ± 3.3 mm/s (26) and 17.5 ± 4.0 mm/s (27) respectively, compared to Takizawa et al. that reported cardiac velocities of ~10 ± 5 mm/s (28). The corresponding respiratory velocities in the same studies were 5.8 ± 4.0 mm/s (26), 6.8 ± 3.4 mm/s (27) and ~3 ± 1 mm/s (28). However, in the study by Yildiz et al. 2022 they consider a single voxel approach that captures peak velocity, rather than average CSF velocities. Wåhlin et al. have reported cardiac stroke volumes at cervical level to be 0.773 ± 0.231 mL (1) while Liu et al. presented values of ~0.6 mL (29), both correspond very well with our estimate. The respiratory stroke volumes at cervical level during guided breathing have been reported to be 0.99 mL in mean and range from 0.54 mL to 1.66 mL (30). Thus, overall, the values obtained in this study appear to be in agreement with previous studies, with the cardiac component slightly higher and the respiratory component slightly lower than the previously reported values. However, these comparisons should be interpreted with some caution, as these effects may vary with age (31), and the participants in our cohort were older than those in the studies used for comparison. Moreover, the breathing *mode* may also affect the CSF modulation (32), where guided breathing potentially increases the effects from respiration. Thus our lower values of the respiratory component may partly be explained by the fact that both Takizawa et al. and Liu et al., utilized guided breathing while the current study used free breathing.

Previous studies have presented an approach to utilize the inflow effect to relate CSF flow and brain activity by calculating the correlation between the CSF signal and global BOLD signal. This method has been successful in linking a reduced coupling between CSF flow and brain activity to neurodegenerative diseases and cognitive decline (15, 16). Nevertheless, these results may not fully capture the absolute magnitudes or the changes in magnitudes of the underlying CSF flow mechanisms, as the correlation measure reflects relative magnitudes rather than providing direct quantitative values. A quantitative approach to estimate CSF flow from the inflow signal has been proposed where the signal equations derived by Gao et al (33) have been used to translate the signal fluctuations to CSF flow (34). However, a limitation with that approach is that it does not capture the oscillating behavior of CSF flow as the signal equations are derived for unidirectional flow and only considers single-slice excitation. Another approach is to use PC-MRI and BOLD fMRI in an interleaved fashion (35), which can capture both flow measurements and the BOLD signal accurately. Such specialized imaging may however not always be feasible (e.g. in ongoing longitudinal aging and dementia studies), whereby a method to retain similar information from standard imaging is desirable. Interestingly, an approach based on spin-ensemble modeling, similar to that presented here but instead using artificial intelligence to translate inflow signal to velocity, has been presented and validated for multislice excitation fMRI data with short repetition times (36), a concept that potentially can be developed to be compatible also with retrospective data-sets.

Limitations. As with all dynamic MRI imaging, the proposed approach is sensitive to motion of the subjects since it induces spin-history changes that are difficult to correct for (37). Because of this, we have excluded participants with high movement during the scanning since they are expected to yield unreliable results for this kind of analysis. The fMRI acquisition is also sensitive to B0 fluctuations which may mainly be affected by respiration. However, the respiratory B0 fluctuations at cervical level 1 and the brain have been shown to be relatively small (38). Moreover, the model assumes the CSF velocity distribution to be well approximated by a plug flow, although the underlying velocity distribution is unknown. However, as simulations showed that the fitted velocities of plug flow display a high correlation to the underlying mean velocities for various flow profiles, the impact of this shortcoming is probably limited. Lastly, Equation 1 does not include a term for the net flow of CSF. Previous research suggests that the CSF production rate in humans is approximately 0.5 mL/min (39). If 50% of the produced CSF is assumed to pass through foramen magnum (40), with an area of 3 cm², the resulting net velocity would be about

0.014 mm/s. Since this net velocity is substantially lower than the oscillatory velocities, it was considered negligible for the model and therefore disregarded in this study to keep the model complexity down. Moreover, the model was only validated using one set of imaging parameters representative of a typical large-scale fMRI datasets. Importantly, we see no intrinsic limitation in the approach that would render the method infeasible for variations in parameter settings (e.g. TR, slice-thickness, slice order, between-slice acceleration).

Conclusion. By modeling spin-history we were able to quantify CSF flow from the inflow effect in fMRI data. The cardiac, respiratory and slow vasomotion flow rates could be separated and cyclic volume variations (i.e. stroke volume) associated with each cycle could be calculated. CSF motion was dominated by the cardiac cycle since this cycle was faster and of greater stroke-volume compared to the other two cycles. Importantly, the proposed method is compatible with all fMRI acquisitions that include cardiac and respiratory recordings, and with an edge slice including the CSF region of interest.

Materials and Methods

Subjects. Sixty-one elderly individuals were randomly selected from the population registry in Umeå Sweden (41). Seven did not complete the fMRI and five were excluded due to poor physiological recordings during the scan (pulse oximeter and respiratory bellows). Thus, the study population consisted of 48 individuals (68-82 years, 19 women). The characteristics are summarized in Table 1. Prior to the MRI scans, all participants underwent a medical examination, during which blood pressure was measured in seated position on the left arm. Relevant medical conditions and medications were also noted. Cognition was tested in all participants using a Montreal Cognitive Assessment (MoCA) test.

The study was conducted according to the ethical principles outlined in the Helsinki Declaration, and the Swedish Ethical Review Authority has approved the study (approval: 2020-03710). Informed consent was obtained both written and orally from all participants. To only include participants who could provide informed consent, a minimum MoCA score of 20 out of 30 possible points was required for participation.

MRI protocol. MRI acquisitions including resting-state fMRI and T_1-weighted volumes were acquired using a 3T scanner (Discovery MR 750; GE Healthcare, Milwaukee, Wisconsin), with a 32-channel head coil. Resting-state fMRI was obtained through a BOLD-contrast sensitive T_2^*-weighted single-shot gradient echo-planar imaging (EPI) sequence. The imaging volumes were collected with 37 axial slices in an interleaved order with a slice sickness of 3.4 mm and 0.5 mm spacing. The imaging parameters were set as follows: repetition time/echo time (TR/TE) 2000/30 ms, flip angle 80°, and field of view (FOV) 25×25 cm^2 with an in-plane resolution of 128×128 voxels. The sequence began with 10 dummy scans so that the magnetization had reached a steady state before any data was collected. Furthermore, physiological recordings including pulse and respiration were collected throughout the scanning period (6 min) by using a pulse oximeter and respiratory bellows respectively.

The T1-weighted volumes were collected using a fast spoiled gradient echo (FSPGR) sequence with the following imaging parameters: TR/TE 8.2/3.2 ms, flip angle 12°, 1 mm slice thickness, in-plane resolution 0.93 mm, FOV 25×25 cm^2 with 176 axial slices, and parallel imaging factor of 2. The MRI acquisitions were part of a quantitative imaging protocol, in which the participants received intravenous contrast injection of gadolinium. T_1-weighted volumes were collected before the injection of gadolinium (Dotarem), whereas the resting-state fMRI acquisition was approximately 3 hours after contrast injection. Gadolinium potentially impacts the BOLD signal, but even if the data is acquired close in time to the injection, its impact on the mean signal change is small (42).

fMRI processing. Before any preprocessing, we manually drew regions of interest (ROIs) in the area of foramen magnum on the bottom slice of the fMRI volume to capture the inflow effect of CSF. The ROIs were divided into two classes based on K-means clustering on the EPI signal to

separate CSF voxels from non-CSF voxels, where the class containing the most voxel was taken to be CSF voxels. This voxel division was visually inspected to verify a representative segmentation of the CSF region. The signal related to CSF movement was then calculated as a spatial average of all CSF voxels, and the resulting time-series was normalized by division of its mean. For the BOLD analysis, realignment, slice timing and co-registration to a high-resolution T1-weighted volume was performed on each fMRI session using SPM12 (43). A whole brain cortical gray matter ROI was created using cortical surface segmentations in FreeSurfer 6.0 (44) and removal of physiological noise was performed using RETROICOR (45). After that, the global BOLD signal in gray matter was extracted from the mean value of all voxels within the gray matter ROI after voxel wise normalization to z-score. The signal was then detrended using a polynomial of degree 2 prior to the application of a band-pass filter (0.01–0.1 Hz). Since high displacements impact the spin history, the framewise displacement was calculated to exclude participants with high movement during the fMRI scan. Here, we excluded participants with a mean framewise displacement greater than 0.5 mm or a maximum framewise displacement greater than 3 mm (N = 5) as motion induced changes in spin history are not considered in the model and may therefore have a negative impact on the fit of the simulated signals.

Modeling CSF dynamics. The CSF dynamics modeling presented in this study is based on the principles of the Monro-Kellie doctrine (18), where the total volume of brain, intracranial blood and CSF is assumed to be constant. This suggests that CSF buffers variations in blood volume by flowing in and out of the spinal compartment, which we want to quantify from the EPI signal fluctuations around foramen magnum, see Figure 1. The intracranial blood volume variations are expected to depend on cardiac pulsations on the arterial side, respiratory variations on the venous side and blood volume variations due to neural activity and autoregulation (vasomotion). Therefore, we constructed a model to mathematically describe the signal fluctuations caused by CSF movement, where the CSF velocity is also assumed to depend on cardiac pulsations, respiratory variations, and slow vasomotion derived from the global BOLD signal. Here, we assumed that the cardiac, respiratory and slow vasomotion components of the CSF velocities are quasi-periodic, captured by the phases calculated from recordings of pulse, respiration and the global BOLD signal.

The phases are calculated with a previously described method that uses the Hilbert-Transform (HT) of a physiological signal to extract the corresponding phases (46), since such approaches can capture nonlinear behavior of oscillatory signals (47). With this method, the cardiac phase (φ_C) was calculated via the HT of the pulse oximetry data after it was shifted by 100 ms due to the delayed triggering of peripheral pulse oximetry. Similarly, the respiratory phase (φ_R) was calculated through the HT of the respiratory bellows data. Lastly, for the slow vasomotion component, we used the timeseries representing the negative derivative of the global BOLD to calculate the phase (φ_{SV}) via the HT, since this derivative should represent the rate of change in cerebral blood volume (14). Using the assumptions above, the CSF velocity over time (t) was written as,

$$v_{CSF}(t) = v_C\cos(\varphi_C(t) + \delta_C) + v_R\cos(\varphi_R(t) + \delta_R) + v_{SV}\cos(\varphi_{SV}(t) + \delta_{SV}), \quad (1)$$

where v_C, v_R, and v_{SV} represent the magnitude of the cardiac, respiratory and slow vasomotion components of the CSF velocity. Moreover, δ_C, δ_R and δ_{SV} are phase shifts between the CSF velocity and the cardiac, respiratory and slow vasomotion phases respectively. The CSF displacement was achieved by integrating v_{CSF}. A least squares estimation of the velocities and phase shifts for each velocity component was acquired by,

$$\boldsymbol{v}, \boldsymbol{\delta} = arg\min_{\boldsymbol{v},\boldsymbol{\delta}} \left\| \boldsymbol{S} - \tilde{\boldsymbol{S}}(v_{CSF}) \right\|_2^2, \quad (2)$$

where $\boldsymbol{S}$ is the measured inflow signal, $\tilde{\boldsymbol{S}}$ is the simulated signal, $\boldsymbol{v} = \{v_C,\ v_R,\ v_{SV}\}$, and $\boldsymbol{\delta} = \{\delta_C,\ \delta_R,\ \delta_{SV}\}$. The optimization problem was minimized using particle swarm (48) with upper and lower bounds on the velocities corresponding to ± 30 mm/s for the cardiac component, and ± 10 mm/s for the respiratory and slow vasomotion components.

Simulations of CSF inflow signal. The simulations began with setting *N* equispaced grid points (i.e. the oscillating ensemble) in a region around the bottom slice of the imaging volume. Each of the grid points were assigned an initial magnetization M_0 along the main magnetic field, representing elements of CSF. After that, the position of each element was updated according to $v_{CSF}(t)$, where a plug flow was used as flow profile of the CSF flow. The inflow effect was simulated by continuously updating the magnetization of moving CSF throughout the fMRI sequence, based on solutions to the Bloch equations (49) and by considering excitation of multiple slices. With the main magnetic field along the z-direction, the initial unperturbed net magnetization is along the z-direction with magnitude M_0. Directly after the application of a radiofrequency (rf) pulse of flip angle θ, the magnetization parallel to the main magnetic field (M_z) and the transverse magnetization ($M_\perp$) become

$$\begin{aligned} M_z^{(1)}(0) &= M_0 \cos(\theta), \\ M_\perp^{(1)}(0) &= M_0 \sin(\theta), \end{aligned} \tag{3}$$

where the superscript indicates the number of rf pulses applied. From the Bloch equations, the relaxation of the magnetizations after rf pulses become

$$\begin{aligned} M_z^{(i)}(t) &= M_0\left(1 - e^{-t/T_1}\right) + M_z^{(i)}(0)e^{-t/T_1}, \\ M_\perp^{(i)}(t) &= M_\perp^{(i)}(0)e^{-t/T_2}, \end{aligned} \tag{4}$$

where T_1 and T_2 are the T1 and T2 relaxation times. A general expression for the parallel and transverse magnetization after *i* rf pulses is

$$\begin{aligned} M_z^{(i)}(0) &= M_z^{(i-1)}(\Delta T_i)\cos(\theta), \\ M_\perp^{(i)}(0) &= M_z^{(i-1)}(\Delta T_i)\sin(\theta), \end{aligned} \tag{5}$$

where ΔT_i is the time between the two succeeding pulses experienced by an element and will be equal to TR only if both excitations occur within the same imaging slice. However, due to CSF motion, the element may undergo excitations in other slices, resulting in ΔT_i differing from TR.

The magnetizations of the elements were updated according to the Equations 3-5 together with the settings of the fMRI sequence, which includes the excitation of multiple slices. At each time step, the parallel magnetization at each position was convolved with a Gaussian kernel corresponding to a dispersion process with a dispersion coefficient of 6 cm^2/min, that is chosen based on the phantom validation, which is in the same order of magnitude as previously reported dispersion coefficient of spinal CSF (25). T1 and T2 values for CSF were set to 4273.4 ms and 1577.6 ms in the simulations, which are based on values from the literature (50). The signal at the bottom slice was acquired by the mean transverse magnetization of all elements localized within the slice, evaluated at TE for each excitation of the bottom slice. Moreover, the simulated signal was normalized by its mean, eliminating the need to determine M_0.

Model validation. The effects of overfitting on the model were examined by fitting the model when interchanging each participant's cardiac, respiratory and slow vasomotion recordings by another participant's recordings. For each participant, the physiological recordings were interchanged with a participant that displayed a low correlation of the physiological recordings, using a metric that was calculated as the maximum absolute cross-correlation between each of the three physiological signals. However, since we want the interchange of gatings to be a permutation, the gatings swaps were therefore performed using Munkres algorithm. The explained variance (R^2) from model fits using swapped recordings were presented with those derived from the true recordings to compare the model's ability to describe the EPI-inflow signal when using both true and false gating data.

The model was further validated using phantoms mimicking oscillatory flow of CSF. Here a hollow cylinder with a length of 9.2 cm and inner/outer diameter of 2.0/4.3 cm was cast in agar (30 g/L) to avoid water/plastic interfaces. An in house developed syringe pump was used to generate oscillatory flow inside the hollow cylinder, which followed a sine-curve with a fixed oscillatory frequency. The frequency of the oscillatory flow was set to 0.93 Hz, 0.23 Hz, and 0.077 Hz respectively to mimic cardiac, respiratory, and slow vasomotion cycles. For the phantom measurements, we used water as flowing medium, and the imaging parameters of the fMRI

acquisitions were the same as the in vivo scan except for the scanning time that was now decreased to 2 min. The evaluation was performed with 6 different velocity amplitudes for each of the three frequencies, chosen to cover the expected physiological velocity ranges, with cardiac velocities ranging between 0 and 20 mm/s, respiratory within 0 and 5 mm/s, and slow vasomotion within 0 and 2.5 mm/s. The simulations of the inflow signal for the oscillating flow in the phantom were repeatedly run with different dispersion coefficients to evaluate the robustness of the model.

The assumption of that a plug flow is representative to the CSF flow profile was validated by simulating signal variations with different flow profiles and fitting a plug flow to the corresponding signal change. Here we simulated signals corresponding to flow profiles of a laminar flow inside a cylinder, and a laminar flow inside an annulus with outer radius 3 times larger than the inner radius, and a plug flow. The simulations were repeatedly run with mean velocities ranging from 1 mm/s to 25 mm/s, and the fitted plug velocities were compared to the mean velocities of the different flow profiles.

Statistics. All statistical analyses were conducted in MATLAB (version 9.13.0. Natick, Massachusetts: The MathWorks Inc.). Normality of the reported variables was assessed using skewness and kurtosis by calculating z-scores, with values within ±1.96 indicating normality. Normal variables are reported as mean ± standard deviation, while non-normal variables are reported with median and interquartile range. Pearson correlation coefficient was used to measure associations between two variables and p-values were considered significant at the 0.05 level.

Author Contributions

Conception of the study (P.S., A.E., J.M., B.A., A.W.); Acquisition and analysis of data (P.S., C.B., A.W.); Writing the first draft of the manuscript and figures (P.S., A.W.); Reviewing and editing the manuscript (all).

Competing Interest Statement

The authors declare no competing interest.

Acknowledgments

This study was supported by grants from the Swedish Research Council (grant number 2022-04263), the Swedish Heart-Lung Foundation (grant number 20210653), and from the Swedish Foundation for Strategic Research (grant number RMX18-0152).

References

1. A. Wåhlin *et al.*, Phase contrast MRI quantification of pulsatile volumes of brain arteries, veins, and cerebrospinal fluids compartments: repeatability and physiological interactions. *Journal of Magnetic Resonance Imaging* **35**, 1055-1062 (2012).
2. V. Vijayakrishnan Nair *et al.*, Human CSF movement influenced by vascular low frequency oscillations and respiration. *Front. Physiol.* **13**, 940140 (2022).
3. A. Kazimierska *et al.*, Compliance of the cerebrospinal space: comparison of three methods. *Acta Neurochir. (Wien.)* **163**, 1979-1989 (2021).
4. A. Wåhlin *et al.*, Assessment of craniospinal pressure-volume indices. *American journal of neuroradiology* **31**, 1645-1650 (2010).
5. M. K. Rasmussen, H. Mestre, M. Nedergaard, Fluid transport in the brain. *Physiological Reviews* **102**, 1025-1151 (2022).
6. J. J. Iliff *et al.*, A paravascular pathway facilitates CSF flow through the brain parenchyma and the clearance of interstitial solutes, including amyloid β. *Science translational medicine* **4**, 147ra111-147ra111 (2012).
7. N. A. Jessen, A. S. F. Munk, I. Lundgaard, M. Nedergaard, The glymphatic system: a beginner's guide. *Neurochem. Res.* **40**, 2583-2599 (2015).
8. H. Mestre *et al.*, Flow of cerebrospinal fluid is driven by arterial pulsations and is reduced in hypertension. *Nature communications* **9**, 4878 (2018).
9. J. J. Iliff *et al.*, Cerebral arterial pulsation drives paravascular CSF–interstitial fluid exchange in the murine brain. *Journal of Neuroscience* **33**, 18190-18199 (2013).
10. B. Ozturk *et al.*, Continuous positive airway pressure increases CSF flow and glymphatic transport. *JCI insight* **8** (2023).
11. S. Dreha-Kulaczewski *et al.*, Inspiration is the major regulator of human CSF flow. *Journal of neuroscience* **35**, 2485-2491 (2015).
12. S. J. van Veluw *et al.*, Vasomotion as a driving force for paravascular clearance in the awake mouse brain. *Neuron* **105**, 549-561. e545 (2020).
13. L.-F. Jiang-Xie *et al.*, Neuronal dynamics direct cerebrospinal fluid perfusion and brain clearance. *Nature*, 1-8 (2024).
14. N. E. Fultz *et al.*, Coupled electrophysiological, hemodynamic, and cerebrospinal fluid oscillations in human sleep. *Science* **366**, 628-631 (2019).
15. F. Han *et al.*, Reduced coupling between cerebrospinal fluid flow and global brain activity is linked to Alzheimer disease–related pathology. *PLoS Biol.* **19**, e3001233 (2021).
16. F. Han *et al.*, Decoupling of global brain activity and cerebrospinal fluid flow in Parkinson's disease cognitive decline. *Mov. Disord.* **36**, 2066-2076 (2021).
17. V. Kiviniemi *et al.*, Ultra-fast magnetic resonance encephalography of physiological brain activity–glymphatic pulsation mechanisms? *Journal of Cerebral Blood Flow & Metabolism* **36**, 1033-1045 (2016).
18. B. Mokri, The Monro–Kellie hypothesis: applications in CSF volume depletion. *Neurology* **56**, 1746-1748 (2001).
19. C. Sudlow *et al.*, UK biobank: an open access resource for identifying the causes of a wide range of complex diseases of middle and old age. *PLoS Med.* **12**, e1001779 (2015).
20. D. M. Barch *et al.*, Function in the human connectome: task-fMRI and individual differences in behavior. *Neuroimage* **80**, 169-189 (2013).
21. B. J. Casey *et al.*, The adolescent brain cognitive development (ABCD) study: imaging acquisition across 21 sites. *Dev. Cogn. Neurosci.* **32**, 43-54 (2018).
22. J.-H. Gao, H.-L. Liu, Inflow effects on functional MRI. *Neuroimage* **62**, 1035-1039 (2012).
23. N. Huotari *et al.*, Sampling rate effects on resting state fMRI metrics. *Front. Neurosci.* **13**, 279 (2019).
24. L.-F. Jiang-Xie, A. Drieu, J. Kipnis, Waste clearance shapes aging brain health. *Neuron* **113**, 71-81 (2025).
25. A. O. Ayansiji *et al.*, Determination of spinal tracer dispersion after intrathecal injection in a deformable CNS model. *Front. Physiol.* **14**, 1244016 (2023).

26. S. Yildiz *et al.*, Quantifying the influence of respiration and cardiac pulsations on cerebrospinal fluid dynamics using real-time phase-contrast MRI. *Journal of Magnetic Resonance Imaging* **46**, 431-439 (2017).
27. S. Yildiz *et al.*, Immediate impact of yogic breathing on pulsatile cerebrospinal fluid dynamics. *Scientific reports* **12**, 10894 (2022).
28. K. Takizawa, M. Matsumae, S. Sunohara, S. Yatsushiro, K. Kuroda, Characterization of cardiac-and respiratory-driven cerebrospinal fluid motion based on asynchronous phase-contrast magnetic resonance imaging in volunteers. *Fluids and Barriers of the CNS* **14**, 1-8 (2017).
29. P. Liu *et al.*, Validating the accuracy of real-time phase-contrast MRI and quantifying the effects of free breathing on cerebrospinal fluid dynamics. *Fluids and Barriers of the CNS* **21**, 25 (2024).
30. C. Gutiérrez-Montes *et al.*, Effect of normal breathing on the movement of CSF in the spinal subarachnoid space. *American Journal of Neuroradiology* **43**, 1369-1374 (2022).
31. T. Vikner *et al.*, CSF dynamics throughout the ventricular system using 4D flow MRI: associations to arterial pulsatility, ventricular volumes, and age. *Fluids and Barriers of the CNS* **21**, 68 (2024).
32. J. M. Kollmeier *et al.*, Deep breathing couples CSF and venous flow dynamics. *Scientific reports* **12**, 2568 (2022).
33. J. H. Gao, S. K. Holland, J. C. Gore, Nuclear magnetic resonance signal from flowing nuclei in rapid imaging using gradient echoes. *Medical physics* **15**, 809-814 (1988).
34. T. C. Diorio *et al.*, Real-time quantification of in vivo cerebrospinal fluid velocity using the functional magnetic resonance imaging inflow effect. *NMR Biomed.*, e5200 (2024).
35. E. C. Roefs, I. Eiling, J. de Bresser, M. J. van Osch, L. Hirschler, BOLD-CSF dynamics assessed using real-time phase contrast CSF flow interleaved with cortical BOLD MRI. *Fluids and Barriers of the CNS* **21**, 107 (2024).
36. B. Ashenagar, D. E. Gomez, L. D. Lewis, Modeling dynamic inflow effects in fMRI to quantify cerebrospinal fluid flow. *Imaging Neuroscience* (2025).
37. E. B. Beall, M. J. Lowe, SimPACE: generating simulated motion corrupted BOLD data with synthetic-navigated acquisition for the development and evaluation of SLOMOCO: a new, highly effective slicewise motion correction. *Neuroimage* **101**, 21-34 (2014).
38. T. Verma, J. Cohen-Adad, Effect of respiration on the B0 field in the human spinal cord at 3T. *Magnetic resonance in medicine* **72**, 1629-1636 (2014).
39. S. Qvarlander, N. Sundström, J. Malm, A. Eklund, CSF formation rate—a potential glymphatic flow parameter in hydrocephalus? *Fluids and Barriers of the CNS* **21**, 55 (2024).
40. M. Edsbagge, M. Tisell, L. Jacobsson, C. Wikkelso, Spinal CSF absorption in healthy individuals. *American Journal of Physiology-Regulatory, Integrative and Comparative Physiology* **287**, R1450-R1455 (2004).
41. T. Vikner *et al.*, Blood-brain barrier permeability, vascular density, and cerebral 4D flow MRI hemodynamics in a population-based elderly cohort. (2022).
42. S. Naganawa, T. Nihashi, H. Fukatsu, T. Ishigaki, I. Aoki, Pre-surgical mapping of primary motor cortex by functional MRI at 3 T: effects of intravenous administration of Gd-DTPA. *Eur. Radiol.* **14**, 112-114 (2004).
43. W. D. Penny, K. J. Friston, J. T. Ashburner, S. J. Kiebel, T. E. Nichols, *Statistical parametric mapping: the analysis of functional brain images* (Elsevier, 2011).
44. B. Fischl, FreeSurfer. *Neuroimage* **62**, 774-781 (2012).
45. G. H. Glover, T. Q. Li, D. Ress, Image-based method for retrospective correction of physiological motion effects in fMRI: RETROICOR. *Magnetic Resonance in Medicine: An Official Journal of the International Society for Magnetic Resonance in Medicine* **44**, 162-167 (2000).
46. P. Söderström *et al.*, Respiratory influence on cerebral blood flow and blood volume – A 4D flow MRI study. *Journal of Cerebral Blood Flow & Metabolism* **0**, 0271678X251316395.

47. B. Kralemann *et al.*, In vivo cardiac phase response curve elucidates human respiratory heart rate variability. *Nature communications* **4**, 2418 (2013).
48. M. R. Bonyadi, Z. Michalewicz, Particle swarm optimization for single objective continuous space problems: a review. *Evol. Comput.* **25**, 1-54 (2017).
49. F. Bloch, Nuclear induction. *Physical review* **70**, 460 (1946).
50. M. Drake-Pérez *et al.*, Normal values of magnetic relaxation parameters of spine components with the synthetic MRI sequence. *American Journal of Neuroradiology* **39**, 788-795 (2018).

Figures and Tables

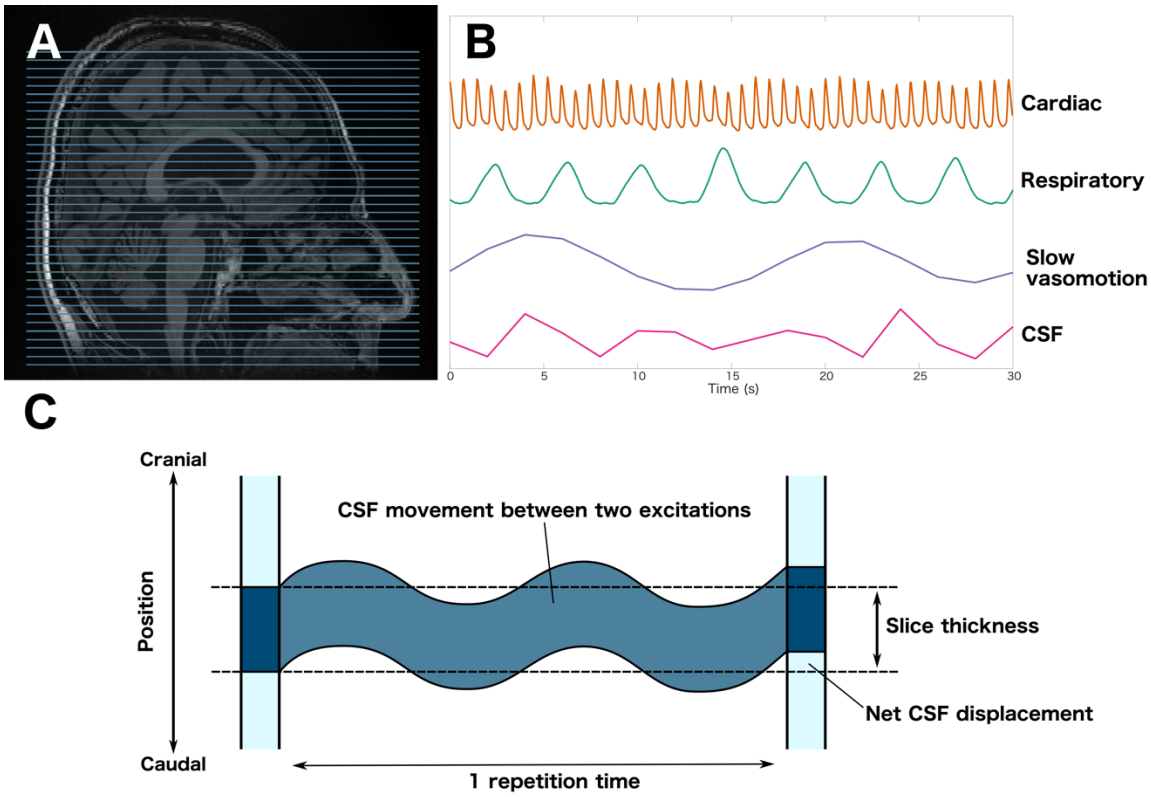

Figure 1. Overview of the fMRI slice positioning, physiological signal extraction, and CSF displacement dynamics during fMRI acquisition. (A) Illustration of the positioning of the 37 slices for fMRI acquisition. (B) Physiological signals that were extracted during the fMRI acquisitions. Cardiac pulsations were measured with pulse oximetry, respiration was measured with respiratory bellows, slow vasomotion was measured from the global BOLD signal, while the CSF signal was measured through the inflow effect at the bottom slice. (C) Illustration of CSF displacement between two subsequent excitations within the same slice when TR = 2 s. Here, one can see that the CSF exchange does not directly reflect the peak velocity between the two consecutive excitations.

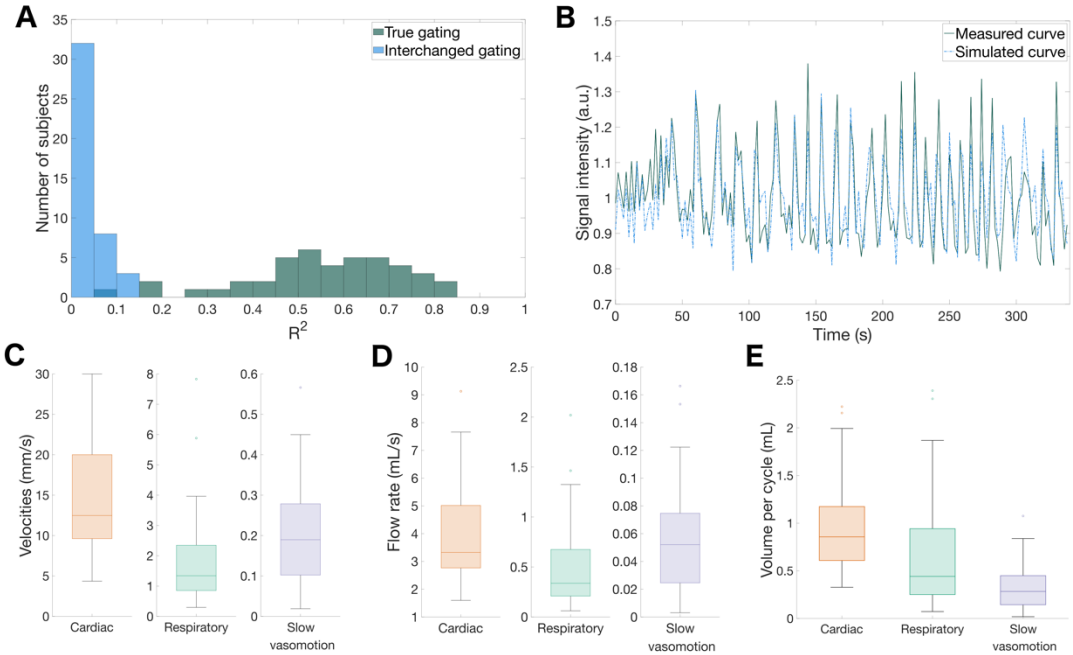

Figure 2. Results from the simulations run on the participants of this study (N = 43). (A) Correlation coefficients between simulated and measured CSF signal for each subject, both with each participants true gating and interchanged gatings. (B) Example fit of the CSF signal. (C) Estimated velocities for each subject and physiological component. Note the different scales on the vertical axes. (D) Estimated flow rates for each subject and physiological component. Note the different scales on the vertical axes. (E) Estimated stroke volumes over each of the physiological cycles for each subject.

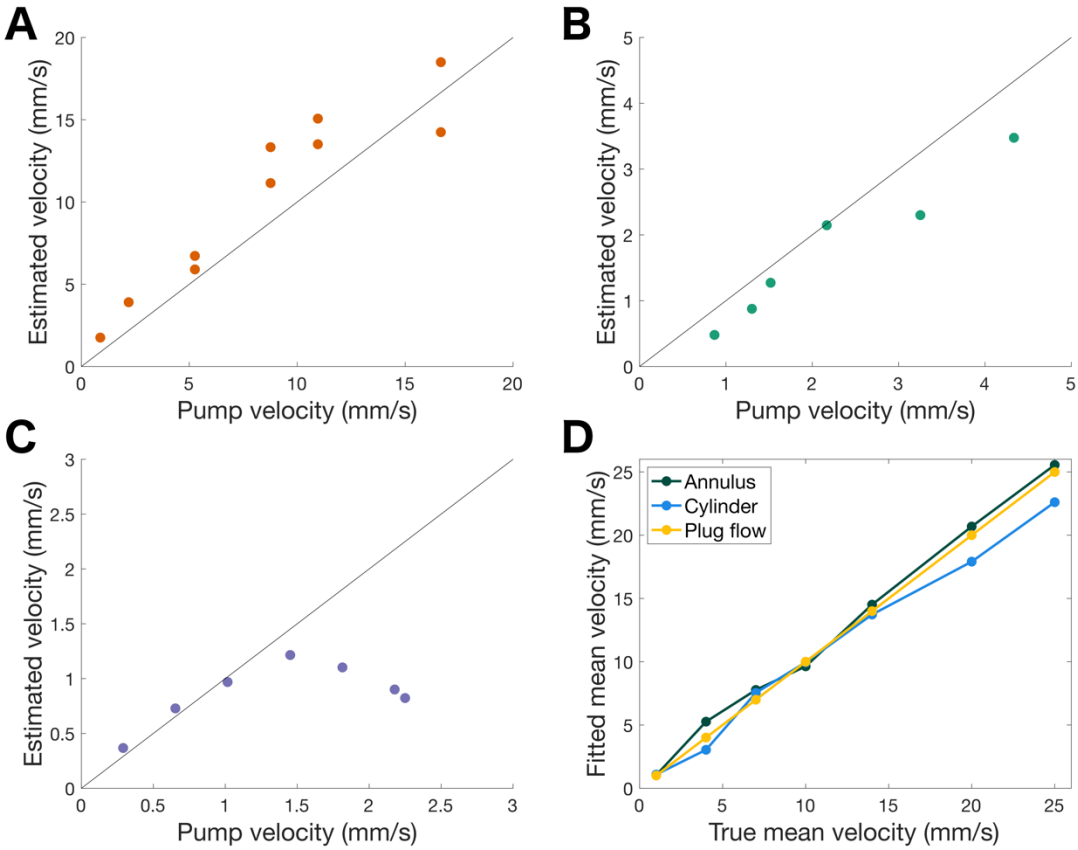

Figure 3. Results from phantom measurements when using a dispersion coefficient of 6.00 cm^2/min. (A) Estimated velocities vs pump velocities for cardiac reflected frequency (0.93 Hz). (B) Estimated velocities vs pump velocities for respiratory reflected frequency (0.23 Hz). (C) Estimated velocities vs pump velocities for slow vasomotion reflected frequency (0.077 Hz). (D) Mean velocities obtained by fitting a plug flow to simulated signals of different flow profiles plotted against the underlying mean velocities.

Table 1. Descriptive characteristics of the participants in this study (N = 48). Categorical variables are given as N (%), while continuous variables are presented with mean ± SD.

Descriptive characteristics of the participants in this study (N = 48). Categorical variables are given as N (%), while continuous variables are presented with mean ± SD.

Age (Years)	76.1 ± 4.0
Sex (Men/Women)	29/19 (60/40)
BMI (kg/m^2)	24.9 ± 3.5
SBP (mmHg)	135 ± 16
DBP (mmHg)	75 ± 10
MoCA score, N (%)	26.2 ± 2.4
Diabetes mellitus, N (%)	6 (13)
Hypertension, N (%)	28 (58)
Hyperlipidemia, N (%)	25 (52)
Atrial fibrillation, N (%)	10 (21)
Transient ischemic attack, N (%)	3 (6)

N, number of participants; SD, standard deviation; BMI, body mass index; SBP, systolic blood pressure; DBP, diastolic blood pressure; MoCA, Montreal Cognitive Assessment

Table 2. Results from phantom measurements when using different values of the dispersion coefficient. The correlation coefficient between estimated and measured fMRI signal (r) and the linear fit with intercept α and slope β are presented for each dispersion coefficient and each operating frequency.

	Cardiac (0.93 Hz)			Respiratory (0.23 Hz)			Slow vasomotion (0.077 Hz)		
Dispersion coefficient (cm^2/min)	**r**	**α**	**β**	**r**	**α**	**β**	**r**	**α**	**β**
2.00	0.9270	1.7316	0.6500	0.9641	0.0148	0.5592	0.5735	0.4308	0.1530
3.00	0.9277	2.0623	0.7445	0.9729	-0.0573	0.6689	0.5685	0.4820	0.1742
4.00	0.9281	2.1183	0.8338	0.9670	-0.0097	0.6959	0.5651	0.5265	0.1842
5.00	0.9214	2.3760	0.8704	0.9682	-0.0493	0.7724	0.5808	0.5423	0.2072
6.00	0.9368	2.2039	0.9504	0.9724	-0.0559	0.8100	0.5767	0.5816	0.2107
7.00	0.9303	2.5455	1.0044	0.9658	-0.0865	0.8539	0.5716	0.6094	0.2193
8.00	0.9207	2.7232	1.0339	0.9598	-0.0124	0.8410	0.5854	0.6179	0.2279